Materials Horizons

ROYAL SOCIETY OF CHEMISTRY

COMMUNICATION

View Article Online
View Journal | View Issue

Cite this: *Mater. Horiz.*, 2026, 13, 2294

Received 5th August 2025,
Accepted 1st December 2025

DOI: 10.1039/d5mh01490e

rsc.li/materials-horizons

Construction of hierarchical 2D/2D few-layered MoS_2/S-doped g-C_3N_4 heterojunctions for enhanced photocatalytic formaldehyde removal

Yihao Duan,[abc] Haihua Wang,[*ab] Guiqiang Fei,[ab] Yu Wang[abd] and Liyu Sun[abe]

Modification of graphitic carbon nitride (g-C_3N_4) with semiconductor nanomaterials has been widely investigated as an effective method to enhance its photocatalytic activity. However, the construction of efficient g-C_3N_4-based heterojunction photocatalysts *via* an environmentally benign method remains critical. Herein, a two-dimensional (2D) few-layered MoS_2/S-doped g-C_3N_4 hierarchical heterojunction was successfully synthesized by a simple strategy *via* combining small molecule-assisted liquid exfoliation, calcination and hydrothermal strategy, which was subsequently utilized for photocatalytic formaldehyde removal. The evaluation of the photocatalytic degradation reaction showed that the as-prepared 2D/2D MoS_2/S-doped g-C_3N_4 photocatalysts exhibited superior photocatalytic activity compared to pristine g-C_3N_4 and S-doped g-C_3N_4 alone, which was attributed to the intimate interface and rapid charge transfer pathways. This heterojunction structure suppresses the excited electron–hole pair recombination within g-C_3N_4, which optimally enhances the photodegradation activity owing to high electron–hole pair separation efficiency. The few-layer MoS_2 nanosheets play an irreplaceable role due to their unique molybdenum–sulfur atomic arrangement, thereby displaying the superior electronic properties of few-layer or even monolayer nanosheets, which make them an important transfer medium for photoexcited electrons. Meanwhile, S doping effectively modulates the band gap of g-C_3N_4 and introduces sufficient structural defects to inhibit electron–hole recombination. Moreover, the synthesis employs efficient and non-hazardous reagents, and the resulting catalysts exhibit outstanding stability and recyclability for pollutant degradation.

New concepts

This work demonstrates a new concept of holistic materials design for high-performance photocatalysts, integrating high-efficiency nanosheet preparation, electronic structure doping, and interfacial heterojunction engineering into a scalable strategy. Unlike conventional approaches that often focus on a single aspect or rely on harmful chemicals, our method uses benign small molecules to exfoliate phase-pure 2H-MoS_2 nanosheets, which are combined with S-doped g-C_3N_4 to create an intimate 2D/2D hierarchical architecture. This synergy provides a dual function: S-doping intrinsically enhances visible-light absorption, while the 2D/2D interface extrinsically establishes ultra-fast charge transfer pathways, collectively boosting the photocatalytic activity for gaseous formaldehyde degradation. The key additional insight for materials science is that exceptional functionality arises from the concerted optimization of material properties across multiple scales—from atomic-level doping to nanoscale interfacial contact. By doing so, this research offers a practical strategy for fabricating high-performance heterojunction photocatalysts, representing a significant advancement toward the efficient utilization of solar energy in the removal of environmental pollutants.

1. Introduction

In-door air pollution has posed a potential risk to human health and safety.[1] Formaldehyde (HCHO) is one of the highly hazardous volatile organic compounds (VOCs) from interior decoration materials and furniture, and is a major source of air pollution.[1,2] Excessive intake and long-term exposure to HCHO can be harmful to the skin and respiratory system, and even cause cancer.[2,3] Therefore, how to effectively remove these low concentrations of harmful air pollutants has become an important direction of research in recent years. Among the various approaches of HCHO removal, semiconductor photocatalysis is recognized as a promising solution due to its simultaneous adsorption and decomposition ability of air pollutants, which can decompose HCHO into CO_2 and H_2O without generating hazardous byproducts.[4–6] Graphite-phase carbon nitride (g-C_3N_4) has attracted increasing attention because of

[a] *Xi'an Key Laboratory of Advanced Performance Materials and Polymers, College of Chemistry and Chemical Engineering, Shaanxi University of Science and Technology, Xi'an 710021, P. R. China. E-mail: whh@sust.edu.cn*
[b] *Shaanxi Key Laboratory of Chemical Additives for Industry, Shaanxi University of Science and Technology, Xi'an 710021, China*
[c] *Xi'an Rare Metal Mediums Institute Co., Ltd, Xi'an 710016, Shaanxi Province, China*
[d] *Xi'an North Huian Chemical Industries Co., Ltd, Xi'an 710302, Shaanxi Province, China*
[e] *School of Materials Engineering, Xihang University, Xi'an, Shaanxi, 710089, China*

its visible light responsiveness and suitable position of band edges.[7] Pure g-C_3N_4 is composed of a stacked coplanar hexagonal heptazine heterocycle structure with weak van der Waals force between the layers. The medium-width band gap electronic structure (2.7 eV) allows excitation upon visible light irradiation, while the good thermal and chemical stability makes g-C_3N_4 a highly desirable candidate for solar photocatalytic applications.[8,9] However, the easy and rapid recombination of photogenerated carriers limits the large-scale application of g-C_3N_4.

Some innovative strategies such as elemental doping,[10] morphology modulation,[11] and heterojunctions[12] were applied to g-C_3N_4 to promote photogenerated electron–hole separation. Doping, the process of incorporating external impurities into a semiconductor, modulates its bulk and surface electronic structure to manipulate conductive, optical, luminescent, magnetic, or other physical properties.[13] In photocatalysis, band gap engineering creates mid-gap doped states by modulating the energy band structure to enhance the light absorption range and reduce the combination of photogenerated electron–hole pairs in pristine g-C_3N_4.[14] Semiconductors can be designed into different dimensions by morphological modulation.[15–18] However, most efforts have focused on investigating the relationship between the morphology and properties of g-C_3N_4. For instance, 0D g-C_3N_4 nanoparticles exhibit shorter charge-transfer length and have rich surface catalytic active sites.[15] 1D g-C_3N_4 nanotubes enhance the separation rate of photogenerated electrons and holes through inner and outer walls.[16] The 2D nanosheet structure of g-C_3N_4 provides a faster electron transfer rate and an extended lifetime of electrons and holes, while the larger specific surface area of the nanosheet itself simultaneously multiplies the number of active sites involved in the reaction.[17] Additionally, 3D porous g-C_3N_4 nanostructures have higher specific surface area and more active sites.[18] Therefore, modulating the morphology is an effective way to improve the catalytic performance of photocatalysts.

Construction of heterojunctions based on heterogeneous coupling theory is also an efficient method to suppress the recombination of photogenerated electrons and holes.[12] The intimate interfacial contact can effectively promote charge separation and transfer, and improve visible light absorption.[19] Usually, the dimensionality and contact type between materials need to be considered when constructing heterojunctions.[20,21] For instance, a 2D/2D heterojunction with extensive interfacial contact facilitates the creation of more migration pathways for photoinduced charges and minimizes charge transfer resistance. Furthermore, the ultrathin 2D/2D heterojunction structure provides abundant catalytic active sites, shortens charge transfer distances, and also enhances light absorption ability.[21,22] Given the advantages of 2D/2D tight interfaces, 2D/2D g-C_3N_4-based heterojunctions have also been extensively fabricated. It has been demonstrated that constructing heterojunctions with g-C_3N_4 boosts its photocatalytic performance, representing a potential strategy for the removal of environmental pollutants.[23] In addition to g-C_3N_4, other semiconductors such as 2D graphene-like materials,[24] 2D transition metal sulfides,[25] 2D metal oxides,[26] 2D bismuth-based semiconductors,[27] *etc.*, are selected to fabricate g-C_3N_4-based 2D/2D heterojunctions. Among them, molybdenum disulfide (MoS_2) is a typical 2D nanomaterial with a layered structure, similar to g-C_3N_4, with an S–Mo–S covalent bond structure connecting each layer by weak van der Waals forces.[28] MoS_2 has a unique electronic structure, exhibiting an indirect bandgap of $\sim$1.29 eV in the bulk form, which transitions to a direct bandgap of $\sim$1.90 eV upon reduction to a monolayer.[29] These characteristic properties make it more effective to functionalize it as a co-photocatalyst in pollutant degradation and photocatalytic hydrogen production.[7,25,30] In addition, the suitable band gap edges, and valence and conduction band positions of MoS_2 nanosheets can be well-matched with g-C_3N_4. The layered structure increases the specific surface area as well as shortens the charge transport time and distance, thereby improving the separation efficiency of photogenerated electrons and holes and enhancing the photocatalytic performance.[7,31] While 2D/2D MoS_2/g-C_3N_4 heterojunctions using few-layered MoS_2 as a synergistic co-catalyst have been reported, their preparation often involves processes that can compromise the intrinsic semiconductor properties of MoS_2, such as lithium-ion intercalation which induces a phase transition to the metallic 1T phase.[7,25,32–37] In this work, we use oleic acid small molecules as intercalators. As a natural fatty acid, oleic acid is non-toxic and environmentally benign, and undergoes complete thermal decomposition at elevated temperatures. Meanwhile, polyvinylpyrrolidone (PVP) is used as a stabilizer to minimize the restacking of MoS_2 nanosheets.

We have synthesized 2D/2D MoS_2/S-doped g-C_3N_4 photocatalyst heterostructures by a combination of facile sonication, calcination and hydrothermal strategy. Sulfur pre-doping extends the visible light response range of g-C_3N_4 and provides sufficient electron capture sites. The prepared heterojunction has a good contact interface for fast charge transfer, thus suppressing the recombination of electron–hole pairs. According to the investigation, this is the first attempt to use a combination of small molecules and polymers to prepare nanosheets and use them for the synthesis of g-C_3N_4-based heterojunction photocatalysts. In addition, studies on g-C_3N_4 photocatalysis have mainly focused on water treatment for degradation of organic pollutants and photocatalytic hydrogen production, with few explorations on the degradation of formaldehyde adsorption in air. We believe that this work will bring new inspiration and expectation to promote and realize industrial production of photocatalysts.

2. Experimental section

2.1. Materials

Melamine ($C_3H_6N_6$), thioacetamide (CH_3CSNH_2), potassium chloride (KCl), and sodium chloride (NaCl) were purchased from Sinopharm Chemical Reagent Co., Ltd. Molybdenum disulfide (MoS_2) (purity $\geq$99.9%) and polyvinylpyrrolidone

(C_6H_9NO) (k30, molecular weight about 40 000) were purchased from Shanghai Maclean Biochemical Technology Co., Ltd. Oleic acid ($C_{18}H_{34}O_2$) and *N*,*N*-dimethylformamide (C_3H_7NO, DMF, >99.9%) were purchased from Shanghai Aladdin Biochemical Technology Co. All materials were analytically pure, and no further purification was required.

2.2. Preparation of sulfur-doped g-C_3N_4

Typically, carbon nitride (g-C_3N_4) was prepared by inducing a condensation reaction of the precursor melamine by high-temperature thermal polymerization. Firstly, 3.5 g of melamine was weighed and washed sequentially with deionized water and ethanol, and centrifugally filtered to remove soluble impurities in the precursor. After dry grinding, 1.5 g of thioacetamide was added with a NaCI/KCI mixed melting salt (the mass ratio of Na salt to K salt is 9 : 11), mixed and ground by using a mortar and pestle for 30 min; then the mixture was added to a crucible with a lid, and the mixed powder was spread flat in the crucible. Then it was placed in a muffle furnace and the temperature was raised to 550 °C in 120 min with a heating rate of 5 °C min^{-1}; the reaction was kept at 550 °C for 180 min, and cooled with the furnace to obtain the yellow product. The product was ground, dispersed in deionized water to dissolve salts, filtered, washed three times, and dried at 50 °C. The sulfur-doped g-C_3N_4 sample was obtained by grinding and sieving and labeled as SCN. Simultaneously, pure g-C_3N_4 was prepared as a control by the same procedure without doping.

2.3. Liquid exfoliation of MoS_2 nanolayers

PVP was dissolved in 50 mL of DMF, and oleic acid was added. Then, 0.25 g of MoS_2 powder was introduced and mixed uniformly by magnetic stirring and sonication for 20 min. The solution was then transferred to a cell pulverizer for 10 h. After crushing, the dispersion was centrifuged at 5000 rpm for 10 min, and then the supernatant was obtained as a MoS_2 nanosheet dispersion. The dispersion was then washed twice with DMF to remove excess PVP and oleic acid. The aqueous MoS_2 nanosheet dispersion was obtained by rotary evaporation using 45% ethanol solution to replace the original solvent DMF, which was repeated three times.

2.4. Preparation of 2D/2D MoS_2/S-doped g-C_3N_4 composite heterojunctions

Few-layered S-doped g-C_3N_4 was obtained by liquid exfoliation of bulk SCN. 1 g of the prepared SCN was weighed and placed in a beaker with 500 mL of deionized water and mixed uniformly with magnetic stirring for 20 min. The sample was then exfoliated by using an ultrasonic cell pulverizer with ultrasonic pulses which was kept at 50 °C for 10 h. The sample was centrifuged at 5000 rpm for 10 min, and the supernatant was collected to obtain the few-layered SCN dispersion. Water was removed by rotary evaporation, and the few-layered SCN powder was obtained by drying and grinding.

0.5 g of SCN and 5 mL of MoS_2 nano-dispersion were placed in a 100 mL PTFE-lined reaction vessel, and then 50 mL of deionized water was added and stirred magnetically for 30 min. The reaction vessel was placed in a constant temperature oven at 140 °C for 12 h and then cooled naturally. The MoS_2 content in the heterojunction was calculated to be 0.5%, 1%, 2% and 3% by adding 2.5 mL, 5 mL, 10 mL and 15 mL of MoS_2 nano-dispersions, respectively. Correspondingly, the samples were labeled as 0.5MS/SCN, 1.0MS/SCN, 2.0MS/SCN, and 3.0MS/SCN, respectively. Fig. 1 briefly shows a schematic diagram of the preparation process.

2.5. Characterization

Micromorphology was checked by using an S-4800 scanning electron microscope (SEM, Hitachi) and a JEM-200CX type transmission electron microscope (TEM, HRTEM, Japan Electronics Co., Ltd). Microstructure was observed using a SPA400-SPI3800N atomic force microscope (AFM, Seiko) in the tapping mode. The phase structure of the product was analyzed by using an Ultima IV X-ray powder diffractometer (XRD, Rigaku). The Raman spectrum of the MoS_2 nanolayers was obtained on a micro confocal laser Raman spectrometer (Raman, Renishaw-invia, THEM).

The structure of g-C_3N_4, SCN and MS/SCN was characterized by VEC-TOR-22 Fourier transform infrared (FT-IR, Bruker) spectroscopy over a wavelength range of 500–4000 cm^{-1}. The photoluminescence spectrum was measured by using an RF-5301PC fluorescence spectrometer (PL, Shimadzu). The UV-vis diffuse reflectance spectrum was obtained on a UV-265FW UV-visible spectrophotometer (UV-vis DRS, Shimadzu). The product structure was analyzed by using an AXIS SUPRA Model X photoelectron spectrometer (XPS, FEI). XPS spectra were processed using a Shirley background subtraction and fitted with mixed Gaussian–Lorentzian (GL(30)) line shapes. ER200DSRC10/12 electron paramagnetic resonance spectroscopy (EPR, Bruker) was utilized to detect free radicals in the reaction process. The sample was tested for valence band and band energy information using ESCALAB 250XI ultraviolet photoelectron spectroscopy (UPS, Thermo Fisher).

The catalyst (5 mg) was dispersed in a mixed solvent of 600 μL of water, 400 μL of ethanol, and 10 μL of 10% Nafion solution to form a uniform ink. 10 μL of ink was transferred and air-dried on an ITO glass to prepare a working electrode. The electrochemical impedance spectroscopy (EIS) measurements were carried out in a conventional three-electrode, single-compartment quartz cell on AMETEK PARSTAT MC 2000 multichannel electrochemical equipment. The sample with an active catalytic area of 4.0 cm^2 on an ITO glass served as a working electrode. A platinum sheet and a saturated calomel electrode (SCE) were used as the counter electrode and the reference electrode, respectively. The photocurrent measurements were performed on the same equipment and using the same working electrode mentioned above. The reference electrode and the counter electrode were a platinum wire and Ag/AgCl respectively, with 0.1 M Na_2SO_4 aqueous solution as the electrolyte. Visible light was generated by a 300 W Xe lamp with an AM 1.5G filter and was chopped manually.

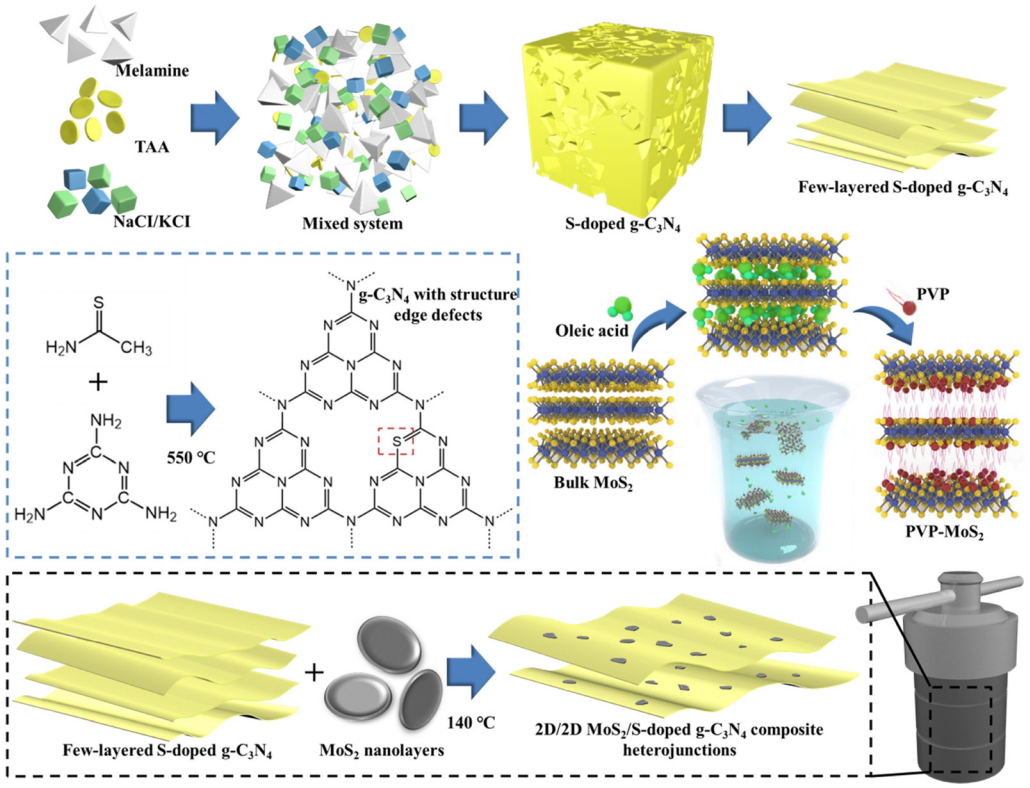

Fig. 1 Schematic diagram of the liquid exfoliation strategy for exfoliating bulk MoS_2 into 2D-MoS_2 nanosheets, the preparation of few-layered S-doped g-C_3N_4, and the construction of 2D/2D MoS_2/S-doped g-C_3N_4 composite heterojunctions.

2.6. Measurement of photocatalytic activity and HCHO removal

Photocatalytic degradation experiments were carried out by using rhodamine B (RhB) and formaldehyde (HCHO). The distance between the light source and the reactor was fixed at 10 cm.

The photocatalytic activity was evaluated by degrading RhB in an aqueous solution under simulated sunlight. To this end, a standard laboratory-scale batch reactor system was utilized. Typically, the reaction was carried out in a 100 mL beaker containing 50 mL of RhB solution (20 mg L^{-1}) and 100 mg of photocatalyst powder, forming a suspension. Before irradiation, the suspensions were ultrasonicated, and then magnetically stirred in the dark for 30 min to establish adsorption/desorption equilibrium. Then, the solution was magnetically stirred and irradiated uniformly with a light source (300 W Xe lamp with an AM 1.5G filter, 100 mW cm^{-2}). The samples were collected every 10 min and absorbance was measured at 553 nm using a UV-265FW spectrophotometer. The concentration (C) of the RhB solution, used to determine the extent of degradation, was calculated according to its absorbance using the Lambert–Beer law:

$$A = KbC \quad (1)$$

where A is the absorbance of RhB solution, K (L (g cm)$^{-1}$) is the absorption coefficient, b (cm) is the thickness of absorption solution, and C (mg L^{-1}) is the concentration of RhB solution.[5]

The degradation rate of RhB was then calculated using eqn (2):

$$W\ (\%) = \frac{C_0 - C}{C_0} \times 100\% = \frac{A_0 - A}{A_0} \times 100\% \quad (2)$$

where C_0 (mg L^{-1}) and C (mg L^{-1}) are the concentration of RhB solution and A_0 and A are the absorbance of RhB solution before and after photocatalytic degradation, respectively.[5]

For the gaseous-phase degradation of HCHO, a custom-made sealed continuous-flow reaction system was used. The reactor consisted of a 500 mL cylindrical quartz vessel. 100 mg of photocatalyst powder was evenly spread in a glass dish placed at the bottom of the reactor. The top of the reactor was sealed with a quartz window for light transmission. Prior to irradiation, the system was shielded with aluminum foil to prevent any light exposure. The reactor was connected to an Innova 1512 infrared photoacoustic gas detector to real-time track the concentrations of HCHO, CO_2, H_2O, and other gas components at 10 min intervals. Initially, ~100 ppm of HCHO gas was injected into the system and allowed to stabilize in the dark to achieve adsorption–desorption equilibrium. The photocatalytic reaction was initiated by removing the aluminum foil and irradiating the catalyst bed uniformly with the same Xe lamp system (300 W Xe lamp with an AM 1.5G filter, 100 mW cm^{-2}).[4] The degradation rate of HCHO was

calculated using eqn (3):

$$W\ (\%) = \frac{C_0 - C}{C_0} \times 100\% \quad (3)$$

where C_0 (ppm) and C (ppm) are the HCHO concentration before and after photocatalytic degradation, respectively.

3. Results and discussion

It is generally believed that the good dispersion of 2D nanomaterials like graphene oxide (GO) in water is attributed to their hydrophilicity, specifically to the presence of hydrophilic groups such as hydroxyl, epoxy and carboxyl groups on the surface, which can produce electrical double layers.[38] The ultrasound-induced exfoliation process results in two main effects: (1) exfoliating the thick bulk material into thin nanosheets and (2) fragmenting larger native flakes to produce nanosheets with small size.[39] On the one hand, the reduction of thickness leads to transitions of intrinsic characteristics (*e.g.* a shift from indirect band gap to direct band gap). On the other hand, fragmentation inevitably breaks the Mo–S bonds on basal planes and the disrupted sites become the edges of the as-prepared MoS_2 nanosheets, thus generating a large number of chemically reactive and unsaturated species.[39] More unsaturated sulfur atoms exposed on the edges can further enhance the photocatalytic efficiency.[40] Meanwhile, the introduction of surfactants can graft more hydrophilic groups on the surface and edges of MoS_2, which can facilitate the formation of stable dispersions in deionized water.[41]

3.1. Morphology performance

The microstructures of the MoS_2 nanolayers and the MS/SCN heterostructure were examined by SEM, TEM and HRTEM (Fig. 2a–h). As shown in Fig. 2a and b, MoS_2 nanosheets with mono- or few layers could be obtained from bulk MoS_2 by the ultrasonication method in a liquid system.[42] The MoS_2 dispersion displays aggregated microstructures comprising a number of thin nanoflakes with lateral dimensions of 100–300 nm. Fig. 2d and e show TEM images of MoS_2 microstructures at low magnification, revealing that they are made up of well-defined and loosely connected flake-like structures. It can be seen that layered structures of MoS_2 are stacked with each other. The edge length of a single MoS_2 flake is ~100 nm, which is well matched with SEM analysis. The typical HRTEM image of the MoS_2 layer is shown in Fig. 2f, where the periodic atom arrangements suggest that the MoS_2 layer is polycrystalline. A typical hexagonal lattice structure with high crystallinity can be observed with the ordered lattice fringe (the (100) plane of hexagonal MoS_2), showing a lattice spacing of 0.276 nm.[23] SEM and TEM images of MS/SCN show that MoS_2 layers are evenly decorated on the g-C_3N_4 substrate and the heterostructure is made up of two different layered materials, as shown in Fig. 2c and g. The layered structure signifies the aggregation of g-C_3N_4 sheets to form plates.[43] MoS_2 is presented as irregular nanoflakes on g-C_3N_4 in the composite samples. The layered MoS_2 co-catalysts are decorated on the surface of g-C_3N_4 to form intimate interfaces, which is favorable for facilitating charge transfer between the semiconductors; hence it is expected to

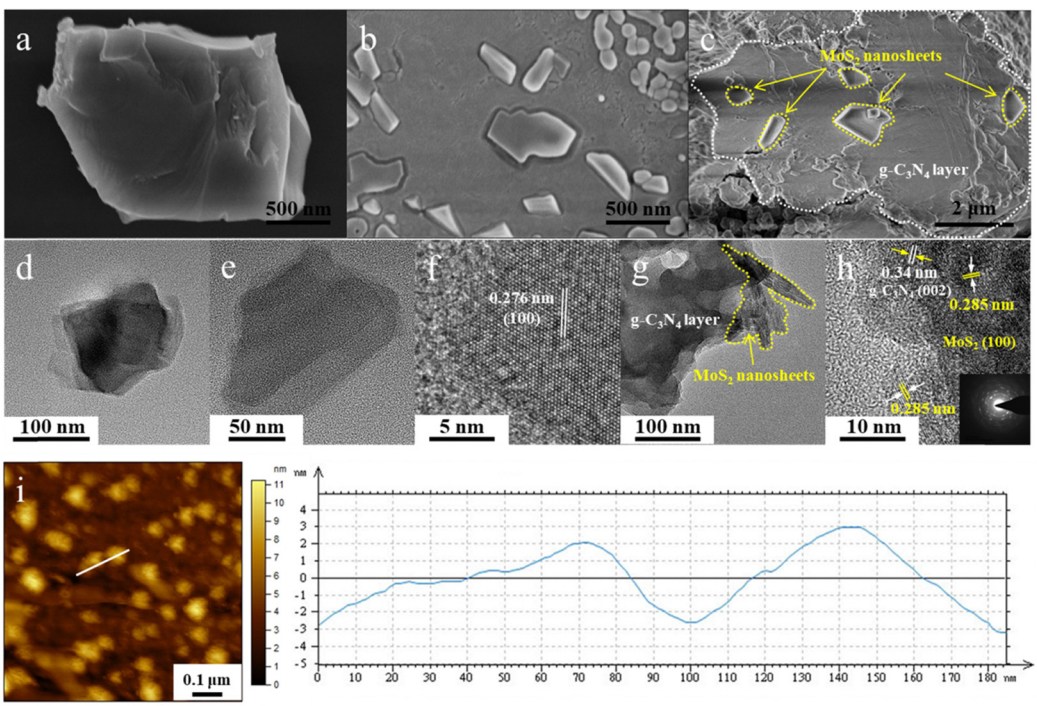

Fig. 2 SEM image of (a) bulk MoS_2, (b) MoS_2 nanosheets and (c) MS/SCN heterostructure. TEM image of (d) bulk MoS_2 and (e) MoS_2 nanosheets. (f) HRTEM image of MoS_2 nanosheets. (g) TEM image of the MS/SCN heterostructure. (h) HRTEM image of the MS/SCN heterostructure. The inset figure shows the SAED pattern for the MS/SCN heterostructure. (i) AFM image of MoS_2 nanosheets and height profile along the white line.

improve the separation of photo-generated charge carriers and therefore the photocatalytic activity.[44] More insights into the structure and morphology have been gained *via* HRTEM analysis of MS/SCN. HRTEM analysis of the MS/SCN heterostructure indicates the presence of MoS_2 on the surface of g-C_3N_4, as shown in Fig. 2h. The image clearly shows the formation of an intimate interface between MoS_2 and g-C_3N_4. The lattice spacing has been observed at 0.285 nm for the (100) plane of hexagonal MoS_2 (JCPDS 37-1492) and 0.34 nm for the (002) plane of hexagonal g-C_3N_4 (JCPDS 87-1526), indicating the formation of a 2D MoS_2/S doped g-C_3N_4 heterojunction.[23,43,45] The inset of Fig. 2h displays the selected area electron diffraction (SAED) pattern for the MS/SCN sample, and the points arranged in multiple hexagons also suggest that the MS/SCN layer stacking is polycrystalline. AFM was performed to further investigate the thickness of the exfoliated MoS_2 nanosheets. Fig. 2i shows the AFM images of the corresponding height profiles of the MoS_2 nanosheets. AFM images and height profile studies clearly show that the nanoparticles are well dispersed with layer thickness in the range of 3–7 nm, indicating the presence of 4–10 layers of MoS_2 nanostructures. The width of individual nanoparticles is about 100 nm, which is consistent with the TEM observations. The AFM, SEM, and TEM results indicate that the MoS_2 nanosheets have been prepared successfully by the liquid exfoliation method and a tight heterojunction interface with g-C_3N_4 is formed.

3.2. Crystal structure and functional group

In order to analyze the functional groups of the as-prepared MS/SCN heterostructure, FTIR spectra were recorded and the results are given in Fig. 3a. With respect to typical g-C_3N_4, the broad band located at 3000–3400 cm^{-1}, involving residual N–H components and O–H bands, was associated with uncondensed amino groups and surface adsorbed H_2O molecules.[46] The peaks located between 1200 and 1650 cm^{-1} correspond to the typical stretching vibration modes of heptazine-derived repeating units. The peaks observed at 1569–1646 cm^{-1} can be attributed to the C=N bonds and the bands observed in the region of 1242–1469 cm^{-1} are typical for C–N in C_3N_4 heterocycles.[46] The sharp absorption peak centered at 810 cm^{-1} is assigned to the characteristic breathing mode of heptazine cycles. Moreover, the weak peak at 883 cm^{-1} can be assigned to the deformation mode of N–H in amino groups.[19] Compared with pure g-C_3N_4, SCN and MS/SCN had similar absorption peaks, which indicated that the introduction of the S element and MoS_2 did not change the basic structure of g-C_3N_4. The emergence of a new absorption band at 2181 cm^{-1} implies the presence of a small number of C≡N bonds in the structure.[46] Moreover, the intensity of the broad peak originally in the region of 3000–3400 cm^{-1} was found to be weakened, indicating that the $-NH_2$ group corresponding to the N–H bond stretching vibration and the –OH group corresponding to the O–H bond vibration were reduced, which implies a more adequate connection between the heptazine rings and a more regular structure.

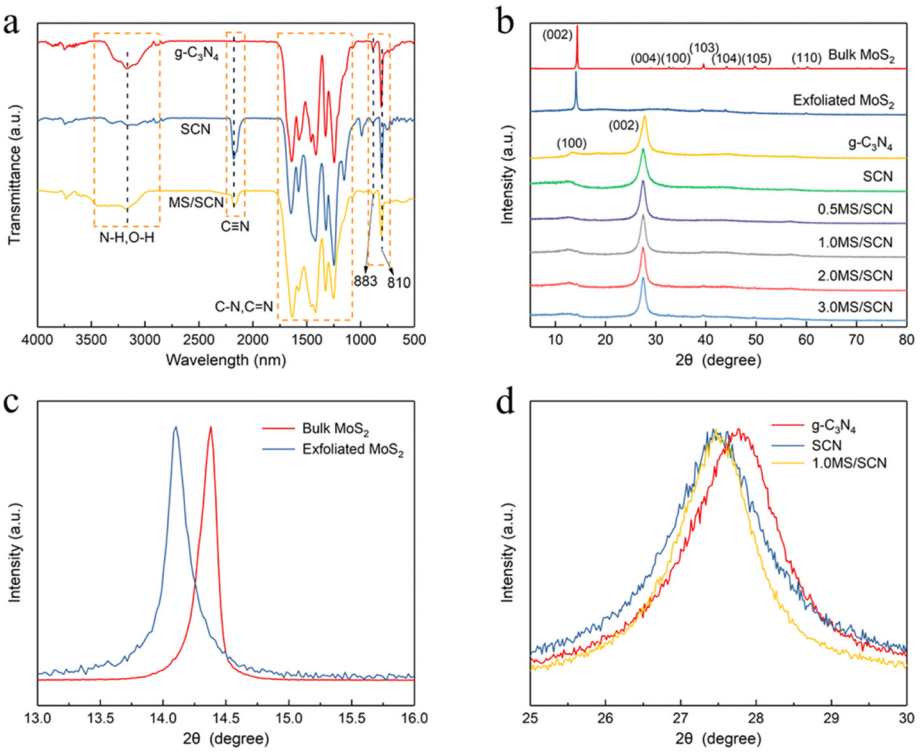

Fig. 3 (a) FT-IR spectra of g-C_3N_4, SCN and MS/SCN. (b) XRD patterns of bulk MoS_2, exfoliated MoS_2, g-C_3N_4, SCN, 0.5MS/SCN, 1.0MS/SCN, 2.0MS/SCN and 3.0MS/SCN. (c) XRD patterns in the range of 13–16°. (d) XRD patterns in the range of 25–30°.

The crystallinity and phase purity of the obtained bulk MoS_2, MoS_2 nanosheets, g-C_3N_4, SCN and MS/SCN heterostructure were analyzed by the XRD technique (Fig. 3b). The bulk MoS_2 shows a strong peak at $2\theta = 14.4^\circ$ and weak peaks at $2\theta = 29.0^\circ$, 32.7°, 39.5°, 44.1°, 49.8° and 58.3°, which correspond to the (002), (004), (100), (103), (104), (105) and (110) planes of MoS_2 (JCPDS no. 37-1492), respectively.[47–49] These peaks match well with the previously reported values for bulk MoS_2.[50] Post exfoliation, there is no difference in the XRD patterns between the bulk MoS_2 and MoS_2 nanosheets except for the peak intensity. Specifically, the peaks corresponding to the (004), (100), and (105) planes essentially disappeared.[47,50] This may be ascribed to the few layered structure compared to a large number of bulk MoS_2, and it indicates the de-stacking of MoS_2 layers.[28,47] The results signify that the crystal structure of MoS_2 is not damaged after the exfoliation process. The (002) peak indicates the stacking of single layers, as shown in Fig. 3c.[28] The full width at half maximum (FWHM) of the (002) peak is 0.15° and 0.22° for bulk MoS_2 and MoS_2 nanosheets, respectively. According to the Debye–Scherrer equation, a broader FWHM corresponds to a smaller crystallite size in the direction perpendicular to the diffraction planes.[48] Therefore, the observed peak broadening directly indicates a reduction in the average stacking thickness along the *c*-axis, confirming the successful exfoliation into few-layered MoS_2 nanosheets.[49] Furthermore, there is a marginal shift to lower angles for the (002) peaks of exfoliated MoS_2. The shift of the (002) peaks to lower angles suggests lattice expansion along the *c*-axis along with the introduction of crystal defects or strains owing to the curvature of the layers. The marginal shift signifies that the lattice distortion is minimal after the exfoliation and hence the structure is relaxed.[28] Fig. 3b also shows the XRD patterns of g-C_3N_4, SCN, 0.5MS/SCN, 1.0MS/SCN, 2.0MS/SCN and 3.0MS/SCN. It can be seen that two diffraction peaks appeared at 13.2° and 27.8°, which can be indexed to the (100) and (002) planes of g-C_3N_4 (JCPDS no. 87-1526) corresponding to the in-plane structural packing motif of tri-*s*-triazine with a distance of 0.683 nm and the interlayer stacking with a distance of 0.321 nm in aromatic segments respectively.[51] These results confirm the formation of g-C_3N_4, SCN and MS/SCN with a typical graphitic, layered structure as in the previous reports.[45] It can be observed that the (100) plane diffraction peak in MS/SCN is slightly weakened compared with SCN, suggesting an interaction between SCN and MoS_2 during formation.[52] Such a case is usually found during the hydrothermal treatment of g-C_3N_4.[53] For the MS/SCN sample, a weak diffraction peak was observed near 39.5°, corresponding to the (103) plane of hexagonal MoS_2. The peak became more prominent with increasing MoS_2 content, suggesting an effective loading of MoS_2 nanosheets and their high dispersion in g-C_3N_4. The XRD pattern of the (002) crystal plane of g-C_3N_4, SCN and 1.0MS/SCN is shown in Fig. 3d. A slight shift from 27.8° to 27.4° occurs in the position of the (002) plane peak during the sulfur doping process. The shift may be due to the presence of sulfur, which enlarges the interlayer spacing of g-C_3N_4. Besides, the full width at half maximum of the diffraction peak became narrower in the MS/SCN heterostructure, indicating that the heterojunction still has high crystallinity, which will facilitate fast electron transport. The corresponding XRD peak positions and relative intensities are summarized in Table S1.

The chemical components and the chemical states of C, N, S and Mo in the MS/SCN heterostructure were investigated by XPS, as shown in Fig. 4. The XPS results (Fig. 4a) indicate that the sample contained elemental C, N, Mo, S and O. Typical peaks could be observed at binding energies of 284.6 eV (C 1s), 398.6 eV (N 1s), 228.6 eV (Mo 3d), 160.6 eV (S 2p) and 530.6 eV (O 1s).[45] The O element may originate from surface absorption and oxidation.[54] The high-resolution XPS spectra of C, N, S and Mo elements are presented in Fig. 4b–e. As observed in Fig. 4b, there are two peaks at about 284.6 eV and 287.5 eV in the C 1s spectrum corresponding to the sp^2 C–C bonds of graphitic carbon and the sp^2-bonded carbon (N═C–N) in the s-triazine rings.[23] Notably, no distinct spectral features for C–O or C═O bonds were identified in the C 1s spectrum, indicating that the

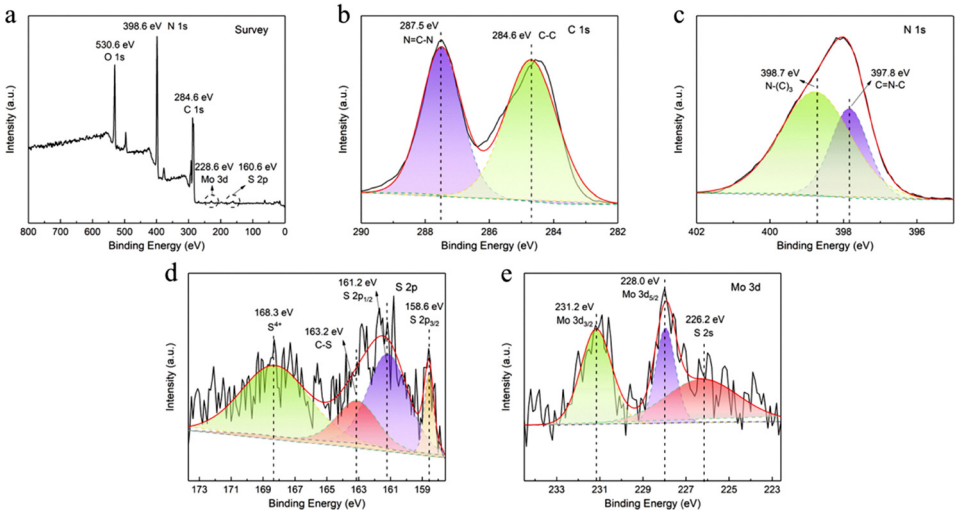

Fig. 4 XPS spectra of (a) MS/SCN. High-resolution XPS spectra of (b) C 1s, (c) N 1s, (d) S 2p, and (e) Mo 3d in MS/SCN.

observed oxygen signal in the survey spectrum is likely due to surface adsorption. Two asymmetrical peaks at 397.8 eV and 398.7 eV can be fitted for the N 1s spectrum in Fig. 4c, which can be ascribed to C=N–C sp^2-bonded N atoms in the graphite-like g-C_3N_4 structure and tertiary (N–$(C)_3$) groups.[45] Sulfur species were further determined from the high-resolution XPS spectrum of S 2p (Fig. 4d). The spectra show binding energies of 158.6 eV and 161.2 eV in accordance with S $2p_{3/2}$ and S $2p_{1/2}$, respectively, indicating the presence of the S^{2-} state in MS/SCN.[55] In addition, the peak at 163.2 eV is attributed to the C–S bond formed by replacing sulfur with lattice nitrogen in the C_3N_4 framework.[55] The peak at 168.3 eV can be assigned to S^{4+} species in sulfate groups (SO_3^{2-}).[56] The high-resolution Mo 3d spectrum in Fig. 4e splits into two main peaks at 231.2 eV and 228.0 eV, which can be assigned to the doublet Mo $3d_{3/2}$ and Mo $3d_{5/2}$, respectively, indicating that Mo in MS/SCN exists mainly as Mo^{4+}. Noticeably, the weak S 2s peak at 226.2 eV also reveals the presence of S^{2-} and Mo^{4+}, which are typical characteristic of MoS_2.[55] The XPS results reveal the formation of a composite material with chemically bound interfaces between g-C_3N_4 and MoS_2.

3.3. Optical properties

Raman spectroscopy can also be used to characterize the thickness of few-layered MoS_2 films.[48] The Raman spectra of bulk MoS_2 and MoS_2 nanosheets are shown in Fig. 5a. Among six vibration modes of MoS_2, only E^1_{2g} and A_{1g} modes are well detected in Raman spectroscopy.[29] The two characteristic Raman peaks of bulk MoS_2 are located at 379 cm^{-1} (E^1_{2g}) and 405 cm^{-1} (A_{1g}), respectively.[48] The E^1_{2g} mode signifies the in-layer displacements of Mo and S atoms and the A_{1g} mode represents the out-of-layer displacements of S atoms along the *c*-axis.[28] The spectra demonstrate that there is a significant red shift in the E^1_{2g} and A_{1g} peaks of MoS_2 nanosheets with respect to the bulk MoS_2. Typically, in the exfoliated MoS_2 nanosheets the A_{1g} mode exhibits red-shift due to the decreased interlayer van der Waals force and the E^1_{2g} mode exhibits blue-shift due to the long-range Coulombic interlayer interactions.[28] However, the MoS_2 nanosheets produced by chemical-assisted exfoliation exhibited red-shift of the E^1_{2g} mode and it was attributed to the adsorption of surfactants, intercalation agents or solvents on the surface of the MoS_2 nanosheets.[28] Because the peak positions of the E^1_{2g} and A_{1g} modes are shifted with respect to the number of MoS_2 layers, the number of MoS_2 layers can be distinguished by the changing spacing between E^1_{2g} and A_{1g} modes in Raman spectroscopy.[29] The spacing between the E^1_{2g} and A_{1g} modes of monolayer, two layer, three layer and bulk MoS_2 is known to be 18–19 cm^{-1}, 22 cm^{-1}, 23–24 cm^{-1} and 25–26 cm^{-1} respectively.[29] Compared to the bulk MoS_2, a red shift of the peak of E^1_{2g} to 385 cm^{-1} could be observed and A_{1g} shows a red shift to 408.5 cm^{-1}, which leads to a decrease in the position difference (Δ) from 26 to 23.5 cm^{-1} between E^1_{2g} and A_{1g}, suggesting the presence of MoS_2 films with three-layer thickness of the nanosheets. The optical properties of the MoS_2 nanosheet dispersions were studied in detail by measuring UV-vis absorption spectra (Fig. 5c). The peaks at 403 nm, 454 nm,

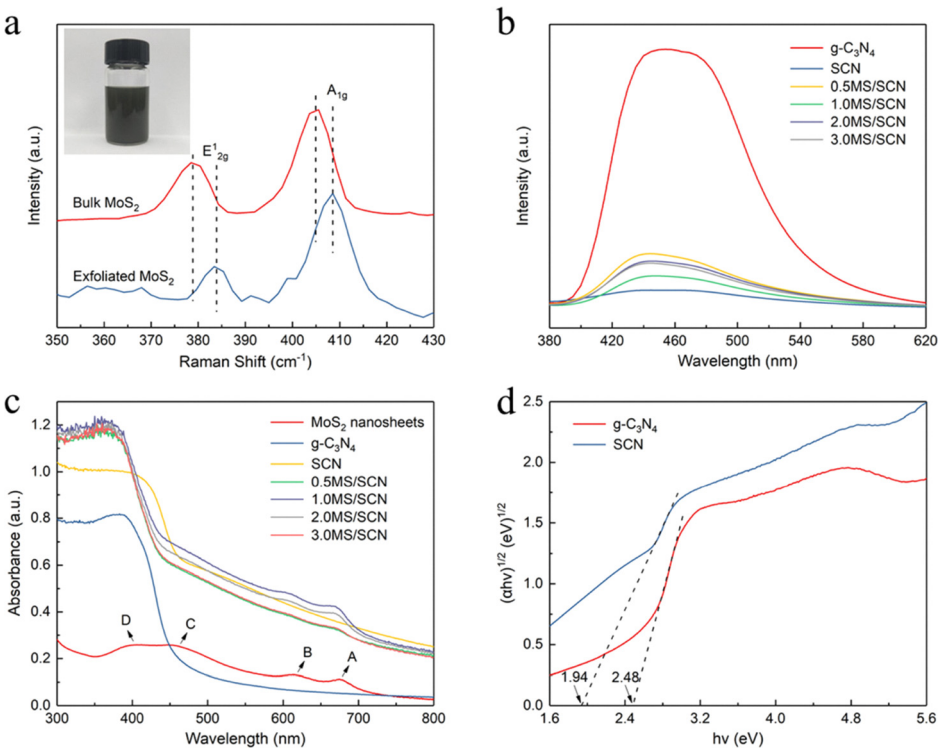

Fig. 5 (a) Raman spectra of bulk MoS_2 and exfoliated MoS_2. The inset figure shows a photograph of MoS_2 nanosheet dispersion. (b) PL spectra of g-C_3N_4, SCN, 0.5MS/SCN, 1.0MS/SCN, 2.0MS/SCN and 3.0MS/SCN. (c) UV-vis spectra of MoS_2 nanosheets, g-C_3N_4, SCN, 0.5MS/SCN, 1.0MS/SCN, 2.0MS/SCN and 3.0MS/SCN. (d) The band gap energy ($h\nu$) of g-C_3N_4 and SCN determined from the $(\alpha h\nu)^{1/2}$ *versus* photon-energy plots.

614 nm, and 674 nm are the characteristic absorption bands of exfoliated MoS_2 in solution. The peaks at 674 nm and 614 nm are ascribed to A and B excitonic peaks, respectively, arising from the K point of the Brillouin zone in 2D MoS_2.[57] And the corresponding color of MoS_2 changes from black to dark green after exfoliation (inset figure in Fig. 5a) because of the direct excitonic transition at the K point of the Brillouin zone.[58] The threshold at ~454 nm (C) and ~403 nm (D) could be attributed to the direct transition from the deep valence band to the conduction band.[57] Additionally, their UV-vis absorption intensities and exfoliation yield gradually increase along with the sonication time (Fig. S1).

The migration of photo-generated e^-/h^+ pairs in g-C_3N_4, SCN, and the MS/SCN composite was investigated by photoluminescence (PL) analysis with an excitation wavelength of 350 nm. The PL spectrum of a semiconductor is related to the recombination of photoinduced charge carriers with its emission photon energy being equal to its band gap energy, as a more intense peak accounts for a more serious recombination.[55,56] As shown in Fig. 5b, all the luminescence spectra of these photocatalysts show a broad peak centered at around 455 nm with a tail extending to 600 nm.[56] SCN and MS/SCN showed a significantly lower PL intensity, and 1.0 MS/SCN had the lowest intensity in the series of heterojunctions. The PL lifetimes decreased with the introduction of sulfur and MoS_2 nanosheets, indicating that the positive role of sulfur in improving the separation efficiency of free charge carriers and the photogenerated electrons of g-C_3N_4 can be efficiently transferred to MoS_2 nanosheets. The formation of the MS/SCN heterojunction effectively slowed down the recombination rate of photoinduced charge carriers, which facilitated the charge transfer at the MoS_2 and SCN interfaces and thus improved the photocatalytic efficiency.[55]

The optical absorption properties and transformed Kubelka–Munk functions *vs.* photon energy of g-C_3N_4, SCN, 0.5MS/SCN, 1.0MS/SCN, 2.0MS/SCN and 3.0MS/SCN composites are also shown in Fig. 5c and d. From Fig. 5c, the absorption edge of pure g-C_3N_4 is at approximately 450 nm; SCN and the MS/SCN composite possess similar absorption patterns. The characteristic absorption peaks A and B of MoS_2 were observed in the MS/SCN composite, which also proved the presence of MoS_2 nanosheets. Compared with the absorption of pure g-C_3N_4 in the visible light region, the absorption intensities of SCN and the MS/SCN composite increased evidently, and presented a remarkable red-shift with an obvious tailed absorption extending to the near-infrared region.[14] This result corresponds to the color change from light yellow to orange to gray after the doping of sulfur into g-C_3N_4 and the coupling with MoS_2.[55] Moreover, the light-absorption ability in the entire spectral range of the composites was gradually enhanced upon increasing the content of MoS_2 nanosheets, and the 1.0MS/SCN sample exhibited the highest absorption intensity, suggesting the contribution of the MoS_2 nanosheets to absorption.[54] The higher visible light absorption of MS/SCN indicates better photocatalytic performance resulting from the more photogenerated electron–hole pairs and the strong electronic coupling between two semiconductors.[51,54]

The band edge positions are important because of their direct effect on the redox reactions occurring at the particle surface.[54] Based on the UV-vis diffuse reflectance spectra, the band gap of semiconductors can be simply calculated using the Kubelka–Munk function equation:[45]

$$(\alpha h\nu)^n = A(h\nu - E_g) \quad (4)$$

where α, ν, A and E_g represent the absorption coefficient, light frequency, proportionality constant and band gap energy, respectively. The transition characteristics of a semiconductor determine the value of n (n = 2 for direct-gap semiconductors and n = 1/2 for indirect-gap semiconductors).[45,51] For g-C_3N_4, the value of n is 1/2.[54] The band gap energies of pure g-C_3N_4 and SCN can be estimated by the transformed Kubelka–Munk functions *vs.* photon energy, as shown in Fig. 5d. The band gap energies of samples are in accordance with the intercepts of the tangent on the x-axis.[51] Thus, the band gaps of as-prepared pure g-C_3N_4 and SCN are estimated to be 2.48 eV and 1.94 eV, respectively. The band gap reduction is about 0.54 eV. The results suggested that the existence of sulfur in SCN enlarged the light absorption width, which could apparently enhance the utilization of visible light.[42]

3.4. Photoelectric properties

Electrochemical impedance spectroscopy (EIS) and transient photocurrent density response were used to investigate the photogenerated charge separation and transfer, as shown in Fig. 6a and b. Fig. 6a is the Nyquist plots of EIS. In general, the smaller arc radius of the EIS Nyquist curve indicates that the interface charge transfer resistance of the working electrode is reduced, which implies efficient separation of photoexcited electron–hole pairs and rapid interfacial charge transfer.[1,4] A decreasing trend of the EIS semicircle was observed as compared to g-C_3N_4 after the doping of sulfur atoms into the system, indicating that elemental doping could facilitate interfacial charge transfer/migration.[13] 1.0MS/SCN exhibits a smaller capacitance arc compared to that of g-C_3N_4 and SCN, suggesting that MoS_2 nanosheets can be functionalized as an electron collector in MS/SCN, and the MS/SCN heterointerface can act as a transporter, thus facilitating the process of interfacial charge transfer.[3]

The enhanced charge transfer rate of 2D/2D MoS_2/S-doped g-C_3N_4 photocatalysts was further demonstrated by the transient photocurrent responses. As shown in Fig. 6b, it was observed that the transient photocurrent density of SCN was higher than that of g-C_3N_4, which was benefited from the smaller resistance of the photocatalysts after the modification, further indicating the advantage of the modification treatment using non-metal elements.[13] 1.0MS/SCN exhibited the highest photocurrent under light illumination, demonstrating an efficient separation of photo-induced electron and hole pairs and a longer electron transfer lifetime at the interface.[30] Moreover, the almost unchanged photocurrent response indicated the excellent stability of the heterojunction. The above mentioned results

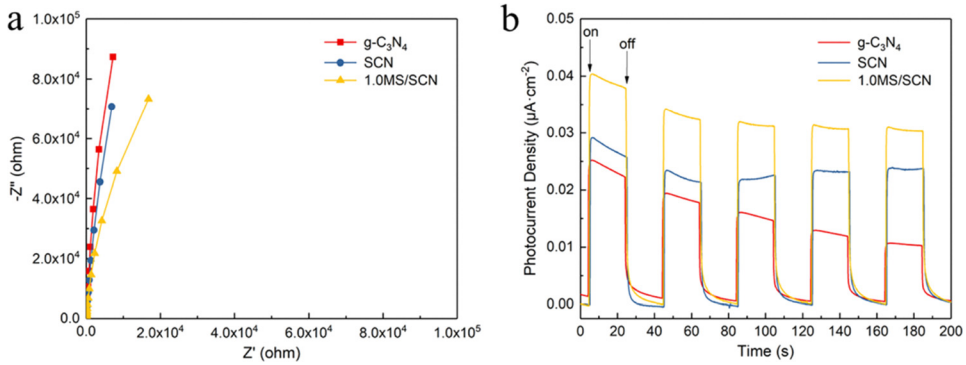

Fig. 6 (a) Nyquist plots of electrochemical impedance spectroscopy of g-C_3N_4, SCN and 1.0MS/SCN. (b) Transient photocurrent density response curve of g-C_3N_4, SCN and 1.0MS/SCN.

demonstrate that the introduction of MoS_2 nanosheets on the surface of S doped g-C_3N_4 could enhance the separation efficiency of photogenerated electron–hole pairs, which can improve the photocatalytic performances.

3.5. Photocatalytic activity

The photodegradation performances were explored using RhB and HCHO as model pollutants under visible light irradiation. Fig. 7a shows the photocatalytic activities of the samples for RhB degradation. Compared with g-C_3N_4, SCN exhibited a much higher degradation rate, which may be ascribed to the doping of sulfur atoms into g-C_3N_4, which can significantly reduce the band gap and extend the optical response range. Moreover, due to the changed local charge distribution and lattice strain, the resulting internal electric field is beneficial for the separation of electron–hole pairs.[14] Furthermore, 2D/2D MoS_2/S doped g-C_3N_4 composites show better photocatalytic activity, indicating that the heterojunction between the MoS_2 nanosheets and the S doped g-C_3N_4 nanosheets is favorable for photocatalytic properties. The photocatalytic activity showed an increasing trend and then a decreasing trend with the increase of MoS_2 content. 1.0MS/SCN shows excellent photocatalytic activity (degradation rate ~95.1%) attributed to the 2D heterojunction structure between MoS_2 nanosheets and g-C_3N_4 nanosheets, which would facilitate the charge transfer between them and further accelerate the separation of electron–hole pairs.[23,55] However, the excessive amount of MoS_2 nanosheets may cover some of the active sites on the surface of the catalyst, thus hindering effective electron transfer from g-C_3N_4. Second, the visible-light absorption ability of MoS_2 is so strong that it might suppress the absorption ability of g-C_3N_4 reducing the photocatalytic degradation efficiency for organic dyes.[59] In this scenario, although the addition of MoS_2 facilitates electron transfer, the total amount of separated electrons from g-C_3N_4 would be suppressed.[59] To further estimate the stability of the as-prepared photocatalyst, a five cycle reusable test was conducted, as shown in Fig. S2. It can be seen that the activity of the catalyst only slightly decreased, and it retained a high level of activity after five repeat cycles under visible-light irradiation. The slight decrease in activity could be due to partial loss of the photocatalyst during the recycling process. The results showed that the as-prepared MS/SCN photocatalyst has good stability during the photocatalytic reaction, and the photocatalyst remained effective for RhB degradation after recycling.

To shed light on the role of the added MoS_2 nanosheets, the kinetics of RhB dye degradation by as-prepared samples was investigated (Fig. 7b). For low-concentration pollutants, the pseudo-first-order kinetic model can be adopted according to the equation[59,60]

$$-\ln\left(\frac{C}{C_0}\right) = kt \quad (5)$$

where C is the concentration of the pollutant (mg L^{-1}) at reaction time t, C_0 is the adsorption equilibrium concentration of the pollutant before irradiation (mg L^{-1}), t is the reaction time (min), and k is the reaction rate constant (min^{-1}). The kinetic constants for g-C_3N_4, SCN, 0.5MS/SCN, 1.0MS/SCN, 2.0MS/SCN and 3.0MS/SCN are 0.01771, 0.03123, 0.01744, 0.04348, 0.02903 and 0.02368 min^{-1}, respectively. With a kinetic constant 2.46 and 1.39 times higher than that of g-C_3N_4 and SCN, the 1.0MS/SCN heterojunction showed enhanced photocatalytic activity, suggesting the existence of a synergistic effect between the components.[59]

Subsequently, the performance of g-C_3N_4, SCN and MS/SCN was evaluated *via* the photocatalytic degradation of formaldehyde (HCHO) under visible light irradiation. In general, CO_2 and H_2O are the final products during the photodegradation process.[61] The photocatalytic results are shown in Fig. 7c. Under visible light irradiation, the pure g-C_3N_4 shows a poor photocatalytic activity and basically no degradation effect on formaldehyde degradation. SCN displays an increased photocatalytic activity with a degradation rate of about 42.2%. Moreover, the MS/SCN samples show a remarkably improved photocatalytic activity compared with g-C_3N_4 and SCN. 1.0MS/SCN shows the best photocatalytic activity, with about 78.1% formaldehyde degradation within 2 h. The monitoring results of the degradation products by 1.0MS/SCN in the gas reactor are shown in Table S2. As the HCHO concentration decreased, the CO_2 content in the system gradually increased, which indicated that HCHO was effectively photodegraded to CO_2

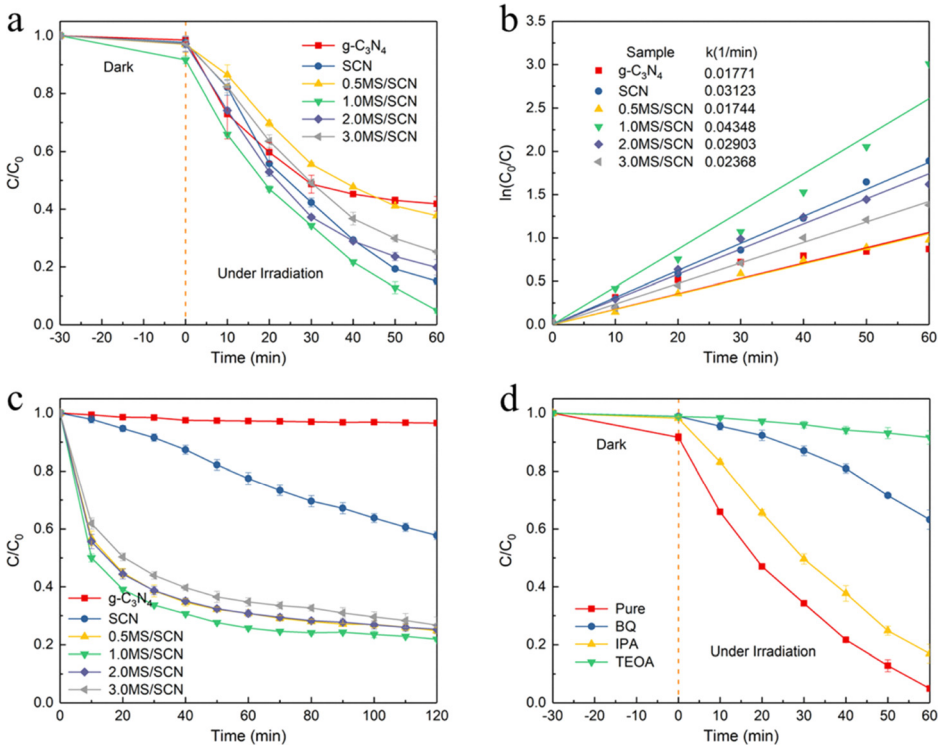

Fig. 7 (a) Photocatalytic degradation of RhB as a function of irradiation time for different samples. (b) First-order kinetic plots of $-\ln(C/C_0)$ *versus* *t* for the photodegradation of RhB. (c) Photocatalytic degradation of HCHO as a function of irradiation time for different samples. (d) Photocatalytic degradation experiments of 1.0MS/SCN in the presence of a radical scavenger.

and H_2O, and a small amount of CO was generated. These photocatalytic results indicate that the deposition of MoS_2 nanosheets on the surface of sulfur doped g-C_3N_4 to form a micro-heterostructure is an effective way for improving the photocatalytic activity of degrading HCHO under visible light irradiation. Furthermore, 1.0MS/SCN exhibits higher photocatalytic reactivity in a shorter time compared to other exquisitely designed g-C_3N_4-based photocatalytic materials, whereas the facile construction enables much easier commercialisation, as reflected in Table 1. The photocatalytic efficiency is reported in terms of percentage removal to facilitate direct comparison with reports in the field. We recognize that

Table 1 Photocatalytic HCHO gas removal using g-C_3N_4-based materials and their experimental conditions and performance in previous studies

Photocatalyst	Irradiation light	Weight of the photocatalyst	HCHO concentration	Reaction time	Decomposition rate (%)	Ref. (year)
Ag/ZSM-5/g-C_3N_4/TiO_2	350 W Xe lamp	0.1 g	1.7 ppm	3 h	93.53	62 (2021)
Bi_2MoO_6/Bi/g-C_3N_4	300 W Xe lamp	0.015 g	200 ppm	10 h	96.15	63 (2020)
Porous g-C_3N_4	LED lamp	0.5 g	0.45 ± 0.01 mg m^{-3}	30 h	56.32	64 (2021)
g-C_3N_4/CeO_2	Fluorescent lamp	0.1 g	180 ppm	7 h	70	65 (2021)
Ag/ZnO/g-C_3N_4	350 W Xe lamp	0.2 g	1.7 ppm	180 min	81.2	66 (2021)
F doped g-C_3N_4	LED lamp	0.1 g	2 μL	240 min	68	67 (2018)
Ag_3PO_4/g-C_3N_4	LED lamp	50 mg	0.5 mg m^{-3}	600 h	22.4	68 (2020)
Biochar/MnO_2/g-C_3N_4	300 W Xe lamp	300 mg	0.5 mg L^{-1}	3 h	91.78	69 (2022)
K–C_3N_4/Ag/$Ag_3PMo_{12}O_{40}$	Visible light (λ > 400 nm)	20 mg	0.16 mg L^{-1}	60 min	60	70 (2021)
TiO_2/g-C_3N_4	500 W LED lamp	0.50 g	5.0 ppm	8 h	89.2	71 (2022)
Ag@g-C_3N_4/ZrO_2	350 W Xe lamp	100 mg	7 ppm	3 h	81.3	72 (2022)
$Bi_2W_xMo_{1-x}O_6$/g-C_3N_4	30 W Xe lamp	200 mg	1 ppm	100 min	92.4	73 (2023)
g-C_3N_4-w	8 W fluorescent lamp	0.1 g	~140 ppm	180 min	66.4	74 (2022)
Hydroxyl-modified/Na-intercalated g-C_3N_4	250 W metal halide lamp	0.2 g	4.5 ppm	105 min	>75	75 (2021)
$BiVO_4$/Bi/g-C_3N_4	300 W Xe lamp	15 mg	800 ppm	6 h	96.39	76 (2020)
Pt/gC_3N_4@CeO_2	8 W fluorescent lamp	0.1 g	~140 ppm	9 h	~84	77 (2021)
$BiFeO_3$@oxygen vacancies g-C_3N_4	Ultraviolet light (365 nm)	100 mg	1.50 ppm	90 min	~54.6	78 (2024)
TiO_2/C/g-C_3N_4	200 W LED lamp	0.3 g	1 mL	8 h	93.7	79 (2025)
g-C_3N_4/Fe_2O_3	50 W LED lamp	0.2 g	1 mg m^{-3}	6 h	65	80 (2023)
TiO_2/g-C_3N_4	300 W Xe lamp	50 mg	2 μL	100 min	~100	81 (2023)
$BiVO_4$/g-C_3N_4/diatomite	300 W Xe lamp (λ > 400 nm)	100 mg	0.02 mL	40 min	81	82 (2024)
MoS_2/g-C_3N_4	300 W Xe lamp	100 mg	~100 ppm	2 h	78.1	This work

normalized removal capacity could provide additional insights in future quantitative mechanistic studies.

Trapping experiments were performed to explore the photocatalytic mechanism of the MS/SCN composites and the effects of different scavengers on RhB degradation (Fig. 7d). In this experiment, *p*-benzoquinone (BQ), triethanolamine (TEOA), and isopropyl alcohol (IPA) were used as scavengers for superoxide radicals ($^{\bullet}O_2^-$), photo-generated holes (h^+) and hydroxyl radicals ($^{\bullet}OH$), respectively.[23,54,60] As shown in Fig. 7d, the photo-degradation efficiency would decrease upon the introduction of any scavenger in RhB systems. The degradation efficiency of RhB under visible-light irradiation decreased significantly when TEOA and BQ were used as the scavenger for h^+ and $^{\bullet}O_2^-$. In contrast, the addition of IPA only slightly affected the photodegradation of RhB, implying that $^{\bullet}OH$ played a relatively minor role in the enhanced photocatalytic performance. Based on these results, it can be concluded that h^+ and $^{\bullet}O_2^-$ are the main oxygen active species for the MS/SCN photocatalyst. Notably, the presence of any scavenger significantly inhibited the dark adsorption of RhB, suggesting that these molecules alter the catalyst–solution interface and compete with the dye for surface sites.

3.6. Photocatalytic mechanism

In order to explore the photocatalytic mechanism of formaldehyde degradation by the MoS_2/S doped g-C_3N_4 nanocomposite, 5,5-dimethyl-1-pyrroline *N*-oxide (DMPO) was added to methanol and water as the trapping agent for superoxide and hydroxyl radicals, respectively. The experiments were conducted without light illumination, followed by a visible-light irradiation period of 5 min. As shown in Fig. 8a and b, no peak signals for DMPO–$^{\bullet}O_2^-$ and DMPO–$^{\bullet}OH$ were observed under dark conditions. Conversely, after 5 min of visible-light irradiation, the methanol-dispersed system of DMPO exhibited a stronger peak signal, whereas the aqueous-dispersed system of DMPO showed a weaker peak signal, indicating that the $^{\bullet}O_2^-$ radicals rather than the $^{\bullet}OH$ radicals played a key role in the photocatalytic reaction. This conclusion aligns with the outcomes of the free radical-trapping experiments.

The band-edge potential position of the composite materials was crucial for the flow of photoexcited charge carriers at the heterojunction, which contributes to explain the mechanism of enhanced photodegradation. The valence band (VB) edge positions of the MoS_2 nanosheets and sulfur doped g-C_3N_4 were estimated using the concept of electronegativity.[54] The valence band (VB) and the conduction band (CB) potentials of a semiconductor can be determined according to the empirical formulas[23]

$$E_{VB} = X - E_e + 0.5E_g \quad (6)$$

$$E_{CB} = E_{VB} - E_g \quad (7)$$

where X is the absolute electronegativity of the semiconductor, computed from the absolute electronegativities of the constituent atoms, and defined as the arithmetic mean of the atomic electron affinity and the first ionizaion energy.[59] The X values for g-C_3N_4 and MoS_2 are 4.67 eV and 5.33 eV, respectively.[23] E_e is the energy of free electrons on the hydrogen scale (about 4.5 eV) and E_g is the band gap energy of the semiconductor.[23] Based on the result of UV-vis spectra, the band gap energy of SCN is 1.94 eV. The band gap energy of MoS_2 nanosheets is 1.90 eV.[23,59] Therefore, the CB and VB of MoS_2 nanosheets were estimated as −0.12 eV and 1.78 eV *vs.* NHE, respectively, and the CB and VB of SCN were estimated as −0.8 eV and 1.14 eV *vs.* NHE, respectively. This result indicates that both the CB and VB positions of MoS_2 nanosheets are more positive than those of SCN and the energy bands are suitable to form a heterojunction.

The valence band maximum (VBM) of the SCN sample was accurately determined by ultraviolet photoelectron spectroscopy (UPS). As shown in Fig. 8c and d, the secondary electron cutoff (E_{cutoff}) and the valence band onset (E_{onset}) were measured from the UPS spectra. The VBM relative to the vacuum level was calculated using the equation E_{VB}, vacuum = $h\nu$ − ($E_{cutoff} - E_{onset}$), where $h\nu$ is 21.22 eV.[83,84] With E_{cutoff} = 17.51 eV and E_{onset} = 1.72 eV, the calculated E_{VB}, vacuum is 5.43 eV. This value was then converted to the normal hydrogen electrode (NHE) scale using the relation E_{VB}, NHE = E_{VB}, vacuum −4.44 eV, yielding a V_{BM} of 0.99 eV *vs.* NHE. This result is in agreement with the empirical value of 1.14 eV estimated from the electronegativity method, with a minor deviation of only 0.15 eV. Combined with the optical band gap (E_g = 1.94 eV) obtained from UV-Vis spectroscopy, the conduction band minimum (C_{BM}) was calculated to be −0.95 eV *vs.* NHE ($C_{BM} = V_{BM} - E_g$). This experimentally derived electronic structure provides a reliable basis for discussing the charge transfer mechanism in the MS/SCN heterojunction.

To better explain the improved photocatalytic performance of MS/SCN, we elaborated the band–band transfer scheme mechanism and potential level (Fig. 8e). When the MoS_2 nanosheets were introduced onto the SCN nanosheets, the two materials closely combined together and a synergistic mechanism was created.[53] Under visible light irradiation, both SCN and MoS_2 were all excited to generate electrons and holes. Based on the energy band position results obtained above, MS/SCN may form conventional type-II heterojunctions or Z-scheme heterojunctions. If the photogenerated charge transfer pathway conforms to the type-II system, since the CB potential of SCN was more negative than that of MoS_2, the photoinduced electrons in the CB of SCN can easily transfer to the CB of MoS_2 through the interface. At the same time, because the VB position of SCN is more negative than that of MoS_2, the holes in the VB of MoS_2 can move to VB of SCN in a similar manner. Therefore, the transfer of photogenerated charges could improve the separation of them. However, for MoS_2, the CB edge potential is more positive than the standard redox potential of $O_2/^{\bullet}O_2^-$ ($E(O_2/^{\bullet}O_2^-)$ = −0.33 eV), and the photoexcited electrons cannot reduce O_2 to $^{\bullet}O_2^-$, which is contrary to the free radical-trapping experiments and EPR test results.[55] Moreover, the VB potentials of SCN and MoS_2 are more negative than the standard redox potential of $OH^-/^{\bullet}OH$ ($E(OH^-/^{\bullet}OH)$ = 1.99 eV) and $H_2O/^{\bullet}OH$ ($E(H_2O/^{\bullet}OH)$ = 2.27 eV), while the VB

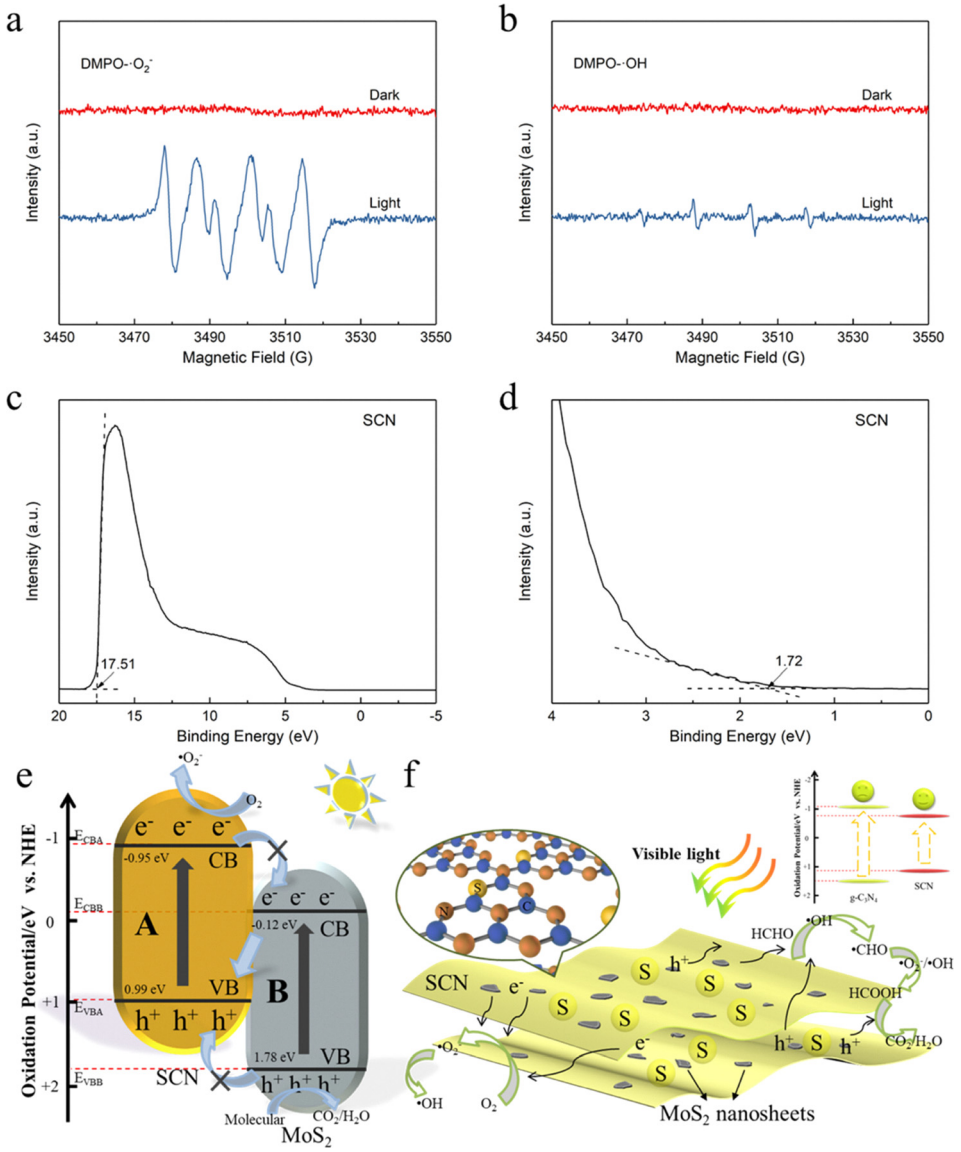

Fig. 8 EPR spectra of (a) DMPO–$^{\bullet}O_2^-$ and (b) DMPO–$^{\bullet}$OH formed in the MS/SCN heterostructure. UPS spectra of SCN: (c) total spectra and cutoff energy region and (d) onset energy region. (e) Electronic band structure and (f) photocatalytic degradation mechanism of pollutants in the 2D/2D MoS_2/S doped g-C_3N_4 system.

holes of SCN and MoS_2 are incapable of oxidizing H_2O or OH^- to $^{\bullet}$OH.[55] Therefore, $^{\bullet}O_2^-$ can only be generated at the CB edge of SCN with more negative potential, which means that MS/SCN is not a type-II heterojunction, but a Z-scheme heterojunction. In this case, the photoinduced electrons in the CB of MoS_2 will recombine with holes in the VB of SCN, while a large number of h^+ exists in the VB of MoS_2. The results show that only a large number of $^{\bullet}O_2^-$ can be produced in the reaction system. These $^{\bullet}O_2^-$ together with the rich h^+ in the VB of SCN acted as the main reactive species to oxidize molecules or pollutants directly. These results are consistent with the free radical-trapping experiments and EPR tests. Therefore, MoS_2 nanosheet incorporation facilitates the electron–hole separation and significantly suppresses recombination, enhancing photocatalytic activity. Moreover, sulfur doping narrows the g-C_3N_4 band gap, extending light absorption into the visible region and increasing photogenerated charge carriers. Enhanced light absorption and increased active sites further contribute to the photocatalytic enhancement.

Based on the above discussion, a possible photocatalytic degradation mechanism of HCHO of 2D/2D MoS_2/S doped g-C_3N_4 is shown in Fig. 8f. The HCHO molecules are adsorbed readily on the g-C_3N_4 matrix by the tri-*s*-triazine (C_3N_3) rings through conjugation and transferred to the surface of the catalyst through molecular diffusion.[53,62] Photons can be absorbed by both MoS_2 and SCN to induce h^+ and e^- on photoexcitation (eqn (8) and (9)). The stored e^- in the CB of SCN can react with the adsorbed O_2 molecules to generate $^{\bullet}O_2^-$ (eqn(10)). And the $^{\bullet}$OH radicals are likely formed further *via* indirect routes from $^{\bullet}O_2^-$ (eqn (10)).[85] Then, the HCHO

molecule reacts with the active group $^{\bullet}OH$, to produce the $^{\bullet}CHO$ radical and water (eqn (11)). $^{\bullet}CHO$ further reacts with $^{\bullet}O_2^-$ and $^{\bullet}OH$ to form HCOOH (eqn (12)). Then HCOOH is oxidized to carbon dioxide and water by the action of valence band h^+ and $^{\bullet}OH$ (eqn (13)).[62] According to the above analysis, the relevant reactions at the heterostructure surface can be expressed as follows:

$$MoS_2 + h\nu \rightarrow h^+ + e^- \quad (8)$$

$$SCN + h\nu \rightarrow h^+ + e^- \quad (9)$$

$$SCN(e^-) + O_2 \rightarrow {}^{\bullet}O_2^- \rightarrow {}^{\bullet}OH \quad (10)$$

$$HCHO + {}^{\bullet}OH \rightarrow {}^{\bullet}CHO + H_2O \quad (11)$$

$$^{\bullet}CHO + {}^{\bullet}O_2^-/{}^{\bullet}OH \rightarrow HCOOH \quad (12)$$

$$HCOOH + h^+/{}^{\bullet}OH \rightarrow H_2O + CO_2 \quad (13)$$

4. Conclusions

In summary, the few-layer MoS_2 nanosheets were fabricated by small-molecule-assisted liquid exfoliation, and 2D/2D few-layer MoS_2/S-doped g-C_3N_4 hierarchical heterojunctions were successfully synthesized by a simple calcination and hydrothermal strategy. The introduction of small molecule intercalators and polymer surfactants was beneficial for fabricating MoS_2 nanosheet dispersions with excellent quality and stability. Compared with pure g-C_3N_4, the addition of sulfur elements effectively reduced the band gap and enhanced light absorption. Most importantly, it is believed that the positive synergetic effect between the sulfur doped g-C_3N_4 and MoS_2 nanosheets as the components of the co-catalyst on the photocatalytic degradation of pollutants can efficiently suppress charge recombination, improve interfacial charge transfer, and provide a greater number of active adsorption sites and photocatalytic reaction centers. The results showed that 1.0MS/SCN had the highest photocatalytic degradation activity of pollutants; the resultant photocatalysts degraded 95.1% of RhB in 1 h and 78.1% of HCHO in 2 h under visible light. A possible mechanism of photocatalytic degradation of HCHO by 2D/2D MS/SCN heterostructures was proposed, in which MoS_2 can accept electrons and SCN can accept holes to generate active $^{\bullet}O_2^-$ and $^{\bullet}OH$ together to enhance the HCHO degradation activity. This study provides a new idea for the batch preparation of MoS_2 nanosheets and demonstrates that two-dimensional structural design is effective for the construction of efficient heterojunction photocatalysts. This provides a more practical strategy for further efficient use of solar energy to remove environmental pollutants.

Author contributions

Haihua Wang and Guiqiang Fei supervised the project. Yihao Duan and Haihua Wang designed the experiments. Yihao Duan and Yu Wang performed the experiments. All authors discussed experiments and results. Yihao Duan, Yu Wang and Liyu Sun wrote the manuscript. Haihua Wang and Guiqiang Fei revised the manuscript. All authors have given approval for the final version of the manuscript.

Conflicts of interest

There are no conflicts to declare.

Data availability

The authors confirm that the data supporting the findings of this study are available within the article and its supplementary information (SI). Supplementary information is available. See DOI: https://doi.org/10.1039/d5mh01490e.

Acknowledgements

This work was supported by the National Natural Science Foundation of China (No. 21978164, 22078189 and 22105120), Outstanding Youth Science Fund of Shaanxi Province (No. 2021JC-046), Special Support Program for high level talents of Shaanxi Province, Innovation Support Program of Shaanxi Province (2021JZY-001), Key Research and Development Program of Shaanxi Province (No. 2020GY-243), Special Research Fund of Education Department of Shaanxi (No. 20JK0535), National High-end Foreign Expert Project (No. GDW20186100428), Key Research and Development Projects of Shaanxi Province (No. 2024SF2-GJHX-19), and Shaanxi Province Qin Chuangyuan "Scientists and Engineers" Team (No. 2024QCY-KXY-127).

Notes and references

1 W. Diao, H. Cai, L. Wang, X. Rao and Y. Zhang, *ChemCatChem*, 2020, **12**, 5420–5429.
2 T. T. T. Vo, H. S. Nguyen, T. T. Tran, P. T. H. Lam, T. T. Nguyen and N. H. Nguyen, *Res. Chem. Intermed.*, 2020, **46**, 4793–4809.
3 M. Chen, H. Wang, X. Chen, F. Wang, X. Qin, C. Zhang and H. He, *Chem. Eng. J.*, 2020, **390**, 124481.
4 X. Li, X. Qian, X. An and J. Huang, *Appl. Surf. Sci.*, 2019, **487**, 1262–1270.
5 C. Hua, X. Liu, S. Ren, C. Zhang and W. Liu, *Ecotoxicol. Environ. Saf.*, 2020, **202**, 110897.
6 S. Kuk, S. Ji, S. Kang, D. Yang, H. J. Kwon, M. S. Koo, S. Oh and H. C. Lee, *Appl. Catal., B*, 2023, **328**, 122463.
7 Y. Yuan, Z. Shen, S. Wu, Y. Su, L. Pei, Z. Ji, M. Ding, W. Bai, Y. Chen, Z. Yu and Z. Zou, *Appl. Catal., B*, 2019, **246**, 120–128.
8 J. Tang, C. C. Er, X. Kong, B. J. Ng, Y. H. Chew, L. Tan, A. R. Mohamed and S. P. Chai, *Chem. Eng. J.*, 2023, **466**, 143287.
9 D. Zhu and Q. Zhou, *Appl. Catal., B*, 2020, **281**, 119474.
10 X. Wu, D. Li, B. Luo, B. Chen, Y. Huang, T. Yu, N. Shen, L. Li and W. Shi, *Appl. Catal., B*, 2023, **325**, 122292.
11 J. Xu, H. Wang, C. Zhang, X. Yang, S. Cao, J. Yu and M. Shalom, *Angew. Chem., Int. Ed.*, 2017, **56**, 8426–8430.

12 Z. Zhang, R. Ji, Q. Sun, J. He, D. Chen, N. Li, H. Li, A. Marcomini, Q. Xu and J. Lu, *Appl. Catal., B*, 2023, **324**, 122276.
13 Z. Lan, G. Zhang and X. Wang, *Appl. Catal., B*, 2016, **192**, 116–125.
14 Y. Li, S. Wang, W. Chang, L. Zhang, Z. Wu, S. Song and Y. Xing, *J. Mater. Chem. A*, 2019, **7**, 20640–20648.
15 L. Wang, G. Zhou, Y. Tian, L. Yan, M. Deng, B. Yang, Z. Kang and H. Sun, *Appl. Catal., B*, 2019, **244**, 262–271.
16 Z. Jiang, X. Zhang, H. Chen, X. Hu and P. Yang, *ChemCatChem*, 2019, **11**, 4558–4567.
17 K. Li, M. Chen, L. Chen, S. Zhao, W. Xue, Z. Han and Y. Han, *Processes.*, 2023, **11**, 528.
18 X. Qian, X. Meng, J. Sun, L. Jiang, Y. Wang, J. Zhang, X. Hu, M. Shalom and J. Zhu, *ACS Appl. Mater. Interfaces*, 2019, **11**, 27226–27232.
19 D. H. Truong, V. Vo, T. V. Gerven and M. E. Leblebici, *Chem. Eng. Technol.*, 2019, **42**, 2691–2699.
20 J. Lu, S. Gu, H. Li, Y. Wang, M. Guo and G. Zhou, *J. Mater. Sci. Technol.*, 2023, **160**, 214–239.
21 X. Zhang, X. Yuan, L. Jiang, J. Zhang, H. Yu, H. Wang and G. Zeng, *Chem. Eng. J.*, 2020, **390**, 124475.
22 J. Sun, C. Wang, T. Shen, H. Song, D. Li, R. Zhao and X. Wang, *Nanomaterials*, 2019, **9**, 907.
23 J. Li, E. Liu, Y. Ma, X. Hu, J. Wan, L. Sun and J. Fan, *Appl. Surf. Sci.*, 2016, **364**, 694–702.
24 R. R. Ikreedeegh and M. Tahir, *Fuel*, 2021, **305**, 121558.
25 K. Zhu, X. Luan, K. M. Postolek and P. Yang, *J. Electroanal. Chem.*, 2021, **893**, 115350.
26 S. Tang, Y. Ma, H. Wang, Y. Liang, X. Xu, D. Zhang, B. Cao, Q. Wang and W. Li, *ChemSusChem*, 2023, **16**, e202202184.
27 B. Wang, D. Chen, N. Li, Q. Xu, H. Li, J. He and J. Lu, *J. Colloid Interface Sci.*, 2020, **576**, 426–434.
28 B. Bindhu, B. K. Sharu, M. S. Gopika, P. K. Praseetha and K. Veluraja, *RSC Adv.*, 2016, **6**, 22026–22033.
29 S. K. Lee, D. Chu, D. Song, S. W. Pak and E. K. Kim, *Nanotechnology*, 2017, **28**, 195703.
30 Z. Wu, X. He, Y. Xue, X. Yang, Y. Li, Q. Li and B. Yu, *Chem. Eng. J.*, 2020, **399**, 125747.
31 Y. Hou, Z. Wen, S. Cui, X. Guo and J. Chen, *Adv. Mater.*, 2013, **25**, 6291–6297.
32 X. Hu, X. Zeng, Y. Liu, J. Lu, S. Yuan, Y. Yin, J. Hu, D. T. McCarthy and X. Zhang, *Appl. Catal., B*, 2020, **268**, 118466.
33 W. Li, L. Wang, Q. Zhang, Z. Chen, X. Deng, C. Feng, L. Xu and M. Sun, *J. Alloys Compd.*, 2019, **808**, 151681.
34 I. W. P. Chen, M. Y. Shie, M. Liu, W. Huang, W. Chen and Y. Chao, *Green Chem.*, 2018, **20**, 525–533.
35 G. Eda, H. Yamaguchi, D. Voiry, T. Fujita, M. Chen and M. Chhowalla, *Nano Lett.*, 2011, **11**, 5111–5116.
36 Z. Lin, Y. Liu, U. Halim, M. Ding, Y. Liu, Y. Wang, C. Jia, P. Chen, X. Duan, C. Wang, F. Song, M. Li, C. Wan, Y. Huang and X. Duan, *Nature*, 2018, **562**, 254–258.
37 Y. Zheng, X. Yin, Y. Jiang, J. Bai, Y. Tang, Y. Shen and M. Zhang, *Energy Technol.*, 2019, **7**, 1900582.
38 T. Shen, S. Hong and J. Song, *Carbon*, 2014, **80**, 560–564.
39 H. Ma, Z. Shen and S. Ben, *J. Colloid Interface Sci.*, 2018, **517**, 204–212.
40 Z. Guo, Q. Ma, Z. Xuan, F. Du and Y. Zhong, *RSC Adv.*, 2016, **6**, 16730–16735.
41 D. Xuan, Y. Zhou, W. Nie and P. Chen, *Carbohydr. Polym.*, 2017, **155**, 40–48.
42 W. Zhang, X. Xiao, Y. Li, X. Zeng, L. Zheng and C. Wan, *Appl. Surf. Sci.*, 2016, **389**, 496–506.
43 P. Fageria, K. Y. Sudharshan, R. Nazir, M. Basu and S. Pande, *Electrochim. Acta*, 2017, **258**, 1273–1283.
44 L. Ge, C. Han, X. Xiao and L. Guo, *Int. J. Hydrogen Energy*, 2013, **38**, 6960–6969.
45 Y. Liu, H. Zhang, J. Ke, J. Zhang, W. Tian, X. Xu, X. Duan, H. Sun, M. O. Tade and S. Wang, *Appl. Catal., B*, 2018, **228**, 64–74.
46 X. Yang, H. Huang, M. Kubota, Z. He, N. Kobayashi, X. Zhou, B. Jin and J. Luo, *Mater. Res. Bull.*, 2016, **76**, 79–84.
47 P. Wu, W. Zhang, Z. Liu and Z. Cheng, *Ceram. Int.*, 2019, **45**, 1730–1736.
48 H. Li, X. Zhang and Z. Tang, *Thin Solid Films*, 2019, **669**, 371–376.
49 H. Dong, D. Chen, K. Wang and R. Zhang, *Nanoscale Res. Lett.*, 2016, **11**, 409.
50 S. Ravula, J. B. Essner and G. A. Baker, *ChemNanoMat*, 2015, **1**, 167–177.
51 X. Lu, Y. Jin, X. Zhang, G. Xu, D. Wang, J. Lv, Z. Zheng and Y. Wu, *Dalton Trans.*, 2016, **45**, 15406–15414.
52 H. Bian, Y. Ji, J. Yan, P. Li, L. Li, Y. Li and S. Liu, *Small*, 2018, **14**, 1703003.
53 M. Joy, B. N. Nair, A. A. P. Mohamed, K. G. Warrier and U. N. S. Hareesh, *Eur. J. Inorg. Chem.*, 2016, 3912–3920.
54 Y. Fu, Z. Li, Q. Liu, X. Yang and H. Tang, *Chin. J. Catal.*, 2017, **38**, 2160–2170.
55 J. Bai, W. H. Lv, Z. Ni, Z. Wang, G. Chen, H. Xu, H. Qin, Z. Zheng and X. Li, *J. Alloys Compd.*, 2018, **768**, 766–774.
56 M. Li, L. Zhang, X. Fan, M. Wu, Y. Du, M. Wang, Q. Kong, L. Zhang and J. Shi, *Appl. Catal., B*, 2016, **190**, 36–43.
57 W. Qiao, S. Yan, X. He, X. Song, Z. Li, X. Zhang, W. Zhong and Y. Du, *RSC Adv.*, 2014, **4**, 50981–50987.
58 C. Zhang, D. Hu, J. Xu, M. Ma, H. Xing, K. Yao, J. Ji and Z. Xu, *ACS Nano*, 2018, **12**, 12347–12356.
59 J. Yan, Z. Chen, H. Ji, Z. Liu, X. Wang, Y. Xu, X. She, L. Huang, L. Xu, H. Xu and H. Li, *Chem. – Eur. J.*, 2016, **22**, 4764–4773.
60 Q. Li, N. Zhang, Y. Yang, G. Wang and D. H. L. Ng, *Langmuir*, 2014, **30**, 8965–8972.
61 Z. Lan, Y. Yu, J. Yao and Y. Cao, *Mater. Res. Bull.*, 2018, **102**, 433–439.
62 W. Wang, D. Zhang, P. Sun, Z. Ji and J. Duan, *Microporous Mesoporous Mater.*, 2021, **322**, 111134.
63 Y. Wu, M. Song, Z. Chai, J. Huang and X. Wang, *ACS Sustainable Chem. Eng.*, 2020, **8**, 7710–7720.
64 L. Kong, X. Li, P. Song and F. Ma, *Chem. Phys. Lett.*, 2021, **762**, 138132.
65 Z. Yan, N. Wang, M. Zhang, M. Xiang and Z. Xu, *J. Environ. Chem. Eng.*, 2021, **9**, 106174.

66 W. Wang, D. Zhang, Z. Ji, D. Shao, P. Sun and J. Duan, *Opt. Mater.*, 2021, **111**, 110721.
67 J. Li, W. Zhao, J. Wang, S. Song, X. Wu and G. Zhang, *Appl. Surf. Sci.*, 2018, **458**, 59–69.
68 X. Rao, H. Dou, D. Long and Y. Zhang, *Chemosphere*, 2020, **244**, 125462.
69 X. Li, G. Fang, X. Qian and Q. Tian, *Chem. Eng. J.*, 2022, **428**, 131052.
70 G. Yan, Y. Gu, P. Qin, W. Deng, M. Lin, C. Huang, Y. Ning, H. Hu and L. Xiao, *Appl. Surf. Sci.*, 2022, **574**, 151693.
71 Y. Wu, D. Meng, Q. Guo, D. Gao and L. Wang, *Opt. Mater.*, 2022, **126**, 112213.
72 J. Duan, X. He, X. Fang, J. Yue, G. Chen and W. Wang, *Diamond Relat. Mater.*, 2022, **129**, 109365.
73 J. Wang, Y. Ding, Q. Dai, W. Zhang, Z. Jiang, Y. Qu, C. Kong, Z. Yang, T. Wang and H. Zhu, *Sep. Purif.*, 2023, **314**, 123551.
74 L. Yue, C. Fang, Z. Yan, Z. Xu, G. Wang and Q. Liu, *J. Environ. Chem. Eng.*, 2022, **10**, 107881.
75 C. Hu, W. F. Tsai, W. Wei, K. Y. A. Lin, M. Liu and K. Nakagawa, *Carbon*, 2021, **175**, 467–477.
76 M. Song, Y. Wu, C. Du and Y. Su, *J. Colloid Interface Sci.*, 2021, **588**, 357–368.
77 G. Huang, Z. Xu, T. Luo, Z. Yan and M. Zhang, *Rare Met.*, 2021, **40**, 3135–3146.
78 B. Di, Z. Wang, H. Wang, S. Gong, L. Zheng, Y. Min and H. Li, *Nano Energy*, 2024, **132**, 110384.
79 A. Khan, R. Jonathan, S. U. Rehman, M. Shoaib, F. Cao, S. Ali, M. Bououdina, P. M. Ismail, J. Wang, H. Abu-Farsakh, Y. Liu and X. Jian, *Arab. J. Chem.*, 2025, **18**, 106034.
80 J. Wang, W. Zhang, H. Wu, F. Su, Q. Dai, Z. Jiang, C. Kong, Z. Yang, T. Wang and H. Zhu, *J. Environ. Chem. Eng.*, 2023, **11**, 109395.
81 Y. Tan, R. Shu, H. Xu, L. Song, R. Zhang, C. Ouyang, M. Xia, J. Hou, X. Zhang, Y. Yuan and R. Zhang, *J. Environ. Chem. Eng.*, 2023, **11**, 110992.
82 L. Xiao, Y. Wang, T. Lei, Z. Yang, J. Yan and D. Jiang, *J. Photochem. Photobiol., A*, 2024, **457**, 115906.
83 K. Sharma, R. Kaushik, S. De, A. Singh, R. Gogoi, B. Das, A. Halder and P. F. Siril, *ACS EST Eng.*, 2024, **4**, 1331–1345.
84 T. Yang, B. Wang, X. Yan, G. Liu, J. Zhao, M. Ji, P. K. Chu, J. Xia and H. Li, *Environ. Chem. Eng.*, 2025, **13**, 115542.
85 X. Wang, W. Xiong, X. Li, Q. Zhao, S. Fan, M. Zhang, J. Mu and A. Chen, *J. Nanopart. Res.*, 2018, **20**, 243.